Journal of The
Electrochemical Society

Analytical Considerations for Hydraulic Resistance Models of the Flow in Electrochemical Cells

To cite this article: S. B. Beale *et al* 2025 *J. Electrochem. Soc.* **172** 054503

Journal of The Electrochemical Society, 2025 **172** 054503

Analytical Considerations for Hydraulic Resistance Models of the Flow in Electrochemical Cells

S. B. Beale,[1,2,z] S. Zhang,[3,z] and A. A. Kulikovsky[1,z]

[1]*Theory and Computation of Energy Materials (IET–3), Institute of Energy Technologies, Forschungszentrum Jülich GmbH, D–52425 Jülich, Germany*
[2]*Mechanical and Materials Engineering, Queen's University, Kingston, K7L 3N6 Ontario, Canada*
[3]*Fundamental Electrochemistry (IET–1), Institute for Energy Technologies, Forschungszentrum Jülich GmbH, D–52425 Jülich, Germany*

The distributed resistance analogy combines local volume-averaging with computational fluid dynamics. It has previously been used to perform three-dimensional calculations for fluid flow (and heat/species/charge transfer) in electrochemical devices such as fuel cell and electrolyzer stacks. These may employ arbitrary-shaped passages, non-uniform local current density, and variable fluid properties. In this paper, the foundation of the distributed resistance methodology is expounded, considering macroscopic and microscopic force and mass balances for plane ducts. Results are presented for the example of the cathode channel of a polymer electrolyte fuel cell. Comparisons are made with analytical and numerical solutions for constant and variable current density along the channel. Distributed resistance analogy and detailed computational fluid dynamics calculations are also compared. Mass transfer through the channel wall leads to additional boundary and inertial effects which alter the value of the distributed resistance. However these effects are shown to be minor for the geometries and current densities encountered in polymer electrolyte fuel cells today. It is concluded that the method forms a sound basis for performance calculations. The work contains information relevant to numerous applications based on hydraulic resistance networks, whenever mass transfer is present.

 [DOI: 10.1149/1945-7111/add183]

Manuscript submitted December 4, 2024; revised manuscript received April 16, 2025. Published May 12, 2025.

Nomenclature

English

$\dot{m}''$	Mass flux, $\mathrm{kg \cdot m^{-2} \cdot s}$
$\hat{F}$	Modified distributed resistance, $\mathrm{kg \cdot m^{-2} \cdot s}$
$\mathrm{F_c}$	Faraday's constant, 96485 $\mathrm{C \cdot mol^{-1}}$
$\overline{j''}$	Mean current density, $\mathrm{A \cdot m^{-2}}$
$\vec{U}$	Superficial or macroscopic velocity vector, $\mathrm{m \cdot s^{-1}}$
$\vec{u}$	Interstitial or microscopic velocity vector, $\mathrm{m \cdot s^{-1}}$
A	Cross-sectional area, $\mathrm{m^2}$
a	Constant term for distributed resistance
B	Channel width, m
b	Linear term for distributed resistance
C_i	Macroscopic concentration, $\mathrm{mol \cdot m^{-3}}$
c_i	Microscopic concentration, $\mathrm{mol \cdot m^{-3}}$
D	Diffusion coefficient, $\mathrm{m^2\ s^{-1}}$
d	"Darcy" resistance in `OpenFOAM`, $\mathrm{m^{-2}}$
D_h	Hydraulic diameter, m
F	Distributed resistance, $\mathrm{kg \cdot m^{-2} \cdot s}$
f	"Forchheimer" term in `OpenFOAM`, $\mathrm{m^{-1}}$
g	Mass transfer coefficient, conductance, $\mathrm{kg \cdot s^{-1}}$
H	Height, m
j''	Current density, $\mathrm{A \cdot m^{-2}}$
J	Diffusion flux, $\mathrm{kg \cdot m^{-2} \cdot} s$
L	Channel length, m
M_i	Molar mass, $\mathrm{kg \cdot mol^{-1}}$
n_D	Net osmotic drag coefficient
P	Macroscopic pressure, Pa
p	Microscopic pressure, Pa
R	Gas constant, 8.314 $\mathrm{J \cdot mol^{-1} \cdot K^{-1}}$
T	Temperature, K
U	Macroscopic velocity component, $\mathrm{m \cdot s^{-1}}$
u	Microscopic velocity component, $\mathrm{m \cdot s^{-1}}$
V	Macroscopic velocity component, $\mathrm{m \cdot s^{-1}}$
v	Microscopic velocity component, $\mathrm{m \cdot s^{-1}}$
V_w	Wall velocity, $\mathrm{m \cdot s^{-1}}$
W	Macroscopic velocity component, $\mathrm{m \cdot s^{-1}}$
w	Microscopic velocity component, $\mathrm{m \cdot s^{-1}}$
x	Displacement component, m
X_i	Macroscopic molar fraction
x_i	Microscopic molar fraction
y	Displacement component, m
Y_i	Macroscopic mass fraction
y_i	Microscopic mass fraction
z	Displacement component, m

Greek

μ	Dynamic viscosity, $\mathrm{kg \cdot m^{-1} \cdot s^{-1}}$
μ_i	Species viscosity, $\mathrm{kg \cdot m^{-1} \cdot s^{-1}}$
ν	Kinematic viscosity, $\mathrm{m^2 \cdot s^{-1}}$
ψ	Stream function, $\mathrm{m^2 \cdot s^{-1}}$
ρ	Density, mixture density $\mathrm{kg \cdot m^{-3}}$
ρ_i	Species density $\mathrm{kg \cdot m^{-3}}$
τ_w	Shear stress, $\mathrm{N \cdot m^{-2}}$

Non-dimensional Numbers

$\mathcal{R}$	Non-dimensional velocity, defined by Eq. 41
λ	Stoichiometric number, $4\mathrm{F_c}X_{\mathrm{O_2}}c_{\mathrm{air}}H/j''L$
$\mathrm{b_M}$	Blowing parameter, $\rho V_w/g^*$, $2V_w/Uc_f^*$
c_f	Friction coefficient, $\tau_w/\frac{1}{2}\rho U^2$
Sh	Sherwood number, $gH/\rho D$
St	Stanton number, $J/\rho U$
Re_{D_h}	Reynolds number, UD_h/ν
Re_W	Wall Reynolds number, V_wH/ν
Re_H	Reynolds number, UH/ν
$\tilde{p}$	Normalized pressure, $(p - p(L))/\frac{1}{2}\rho U(0)^2$
$\tilde{x}$	Normalized displacement, x / L
$\tilde{y}$	Normalized displacement, y / H
$\tilde{V}_w$	Non-dimensional wall velocity, $V_w/U(0)$
f	Berman's f-function

[z]E-mail: s.beale@fz-juelich.de; s.zhang@fz-juelich.de; a.kulikovsky@fz-juelich.de

In process engineering, a problem often arises when building computational models of equipment such as electrochemical cells and stacks (fuel cells, electrolyzers, batteries etc...), made up of hundreds or thousands of components, where it is not feasible to construct a computational mesh that is both large enough to tesselate the entire region, and at the same time fine enough to capture the detailed motion of the chemical species locally.

In pioneering work, Patankar and Spalding[1] considered a 3-D computational model of a shell-and-tube heat exchanger, where the coarse motion describing the flow of mass and heat around the baffles of the heat exchanger was obtained by computation, but the fine details of the flow around the individual tubes were modeled, based on the hydraulic resistance, denoted by F, and a volumetric heat transfer coefficient. Following this, several authors employed the methodology for application to heat exchangers and other devices.[2–7] Patankar and Spalding referred to the approach as a "distributed resistance analogy" (DRA). Others refer to a "macro-homogeneous" model, and also a "porous media analogy", based on the theory of percolation (creeping flow) in random assemblies, which is governed by Darcy's law.[8] However, the mathematical description of the resistance or drag, in more commonly encountered flow regimes where inertial effects may be significant, is generally attributed to the pioneering work of Reynolds.[9]

Beale and Zhubrin[10] extended the DRA approach for prediction of performance in fuel cell stacks. The channels were treated as plane ducts, an assumption that is perfectly reasonable for the anode/fuel electrode in many planar solid oxide cell designs. The DRA results were compared with those obtained from a detailed numerical model (DNM).[a] Further improvements were to come in more recent works,[11–13] where the channels were treated as rectangular ducts. Zhang[14] further extended the approach to consider two-phase flow in polymer electrolyte fuel cell stacks with inter-phase heat and mass transfer. He et al.[15,16] developed a reduced model for a solid oxide fuel cell (SOFC) stack.

With advances in computational capabilities, high-fidelity numerical simulations have become increasingly feasible.[17] Nonetheless, reduced-order models remain essential for enabling rapid predictions and facilitating the analysis of large-scale energy conversion systems, such as SOFC and solid oxide electrolyzer cell stacks and systems,[18–23] as well as proton exchange membrane fuel cell (PEMFC) stacks and systems.[24–26] These simplified models are particularly valuable for addressing practical engineering issues, including flow maldistribution,[27] and are increasingly applied in domains such as heavy-duty transportation[28] and unmanned aerial vehicles.[29] Within these complex systems, distinct parts fulfill critical functions.[30] For instance, heat exchangers are vital for transferring thermal energy between cold inlets and hot outlets, reaction zones are designed to support efficient electrochemical and chemical transformations, and manifolds serve to optimize flow and temperature uniformity across the device. To further enhance the predictive capabilities and generalizability of reduced models, current research is actively exploring the integration of machine learning techniques to capture system behavior across a wide range of operating conditions.[31] Despite their widespread application, it remains essential to critically evaluate the accuracy and inherent limitations of reduced-order models when applied to real-world scenarios.

Pressure gradients in fuel cell and electrolyzer stacks are extremely important: Should these vary substantially from channel-to-channel then flow maldistributions will occur. These can adversely affect the delivery and removal of reactants and products to the reaction sites, and thereby the local current density. Therefore, accurate prediction of the pressure losses in the channels and elsewhere, such as in the stack headers and porous transport layers, if present, is very important in electrochemical design.

One important difference between the flow fields in electrochemical systems and the earlier heat exchanger work[1] is the presence of mass transfer effects due to finite-rate electrochemical reaction(s), i.e., sources and sinks of matter through the channel wall. This has two immediate effects (i) the frictional resistance at the wall(s) is increased/reduced owing to mass transfer,[32] i.e., boundary layer or diffusion modifications and (ii) inertial effects due to added or reduced mass, which tend to accelerate or decelerate the flow, i.e., change the bulk velocity (and in some cases density). The implications of these additional processes are discussed below. Other mass transfer applications where the DRA could be readily employed, include membrane separations technology,[33–35] where hundreds or thousands of spacers may be employed in conventional filtration devices such as plate-and-frame and spiral configurations, the headers of fuel cells/electrolyzers where a DRA-type hydraulic model is frequently employed, and more generally in numerous application based on hydraulic resistance networks, where mass transfer is present.

Validation and verification are important steps in proving the utility of numerical code sequences. While physical experiments are practically irreplaceable in terms of validation of the results of calculations and the general precision of obtained results, analytical methods can and should also be readily employed to verify the mathematics of closure methods such as the DRA, under canonical conditions. This is important as it can show the precision of the particular scheme employed.

'While mathematical correctness does not imply physical validity, the latter cannot be obtained without the former.'

Drew and Passman[36]

This paper is concerned with a comparison between numerical models and analytical solution methods. It is important to appreciate, from the outset, the difference between a *macro-scale* and a *micro-scale* formulation. In this article, macroscopic (volume-averaged) quantities are denoted by capital roman letters,[b] U, V, P, Y_i, etc..., whereas microscopic (local) values are represented by lower case roman symbols, u, v, p, y_i, etc... In the *micro-scale* both streamwise velocity, $u(x, y, z)$, and crosswise velocities and $v(x, y, z)$, $w(x, y, z)$, are present, even if v is generally much smaller than u. These may be considered local values at some point (x, y, z) in space (Fig. 1). For the quasi 2-D problem of duct flow, volume-averaging may be considered equivalent to area-averaging in the transversal y-z plane (rectangular ducts) or simply integrating/averaging in the y direction (plane ducts). Injection/suction occurs at specific locations such as $y = \pm H$. For the *macro-scale* formulation,[c] only the bulk value of $U = U(x)$ is considered in 1-D due to streamwise averaging; Normally, $U = \bar{u}$, $V = \bar{v} = 0$, $W = \bar{w} = 0$, and $dP/dy = dP/dz = 0$. The overbar denotes averaging in the cross–wise y direction, for some variable ϕ.

$$\bar{\phi} = \frac{1}{H}\int_0^H \phi dy \qquad [1]$$

For the macroscopic realization, the location of injection/suction is not generally prescribed, and rather may be considered as a source/sink per unit volume resulting only in a change in the streamwise U velocity as a function of x. Here, the macroscopic length-scale is that of the duct height, H, or hydraulic diameter, D_h, whereas the microscopic scale is 1-2 orders-of-magnitude smaller. The implications of the existence of these two distinct length scales are discussed further below.

[a] In the fuel cell modeling literature the abbreviation "DNS" is sometimes used to denote direct numerical simulation of transport in porous media. The reader will note the difference with the present terminology, "DNM", which is consistent with that employed in previous works on stack modeling.

[b] However, for the sake of brevity, and at the risk of inconsistency, we shall *not* adopt this convention for properties, so that, for example, ρ is density in both macro-scale and micro-scale formulations.

[c] This is for the 1-D analysis in this document. For the 3-D DRA method[13] used in CFD, V and W are not necessarily zero, but rather describe the "gross" motion of the gas(es).

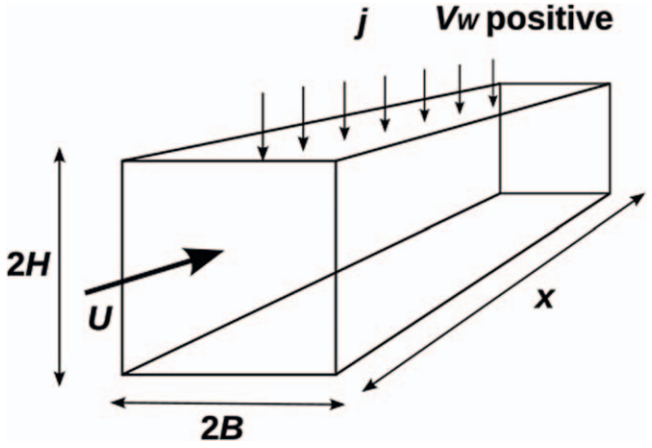

Figure 1. Geometry and nomenclature for rectangular duct. In this case, mass transfer occurs at only one of the four lateral boundaries. For a plane duct $B \gg H$ (Jorne's problem). N.B.: In the present work, V_w is positive for mass injection and negative for suction.

Macroscopic Formulation

Basic equations.—The macroscopic equation of momentum was given by Patankar and Spalding[1] as follows;

$$\rho\frac{\partial\vec{U}}{\partial t} + \rho\vec{U}\cdot\vec{\nabla}\vec{U} = -\vec{\nabla}P - F\vec{U} \qquad [2]$$

where $\vec{U} = (U, V, W)$ is a superficial or filter velocity, ρ is the partial density of the fluid (thereby accounting for the fact that space contains multiple fluids and solids). Attention is confined to situations where the transient term $\partial\vec{U}/\partial t = 0$. The distributed resistance, F, may be obtained from:

(i) Analytical solution (for a simple geometry)
(ii) Experimental data
(iii) Detailed computer calculations

or a combination of these methods. A typical combined analytical/numerical approach would be the use of a computer to enumerate eigenvalues of a Sturm–Liouville system of equations, obtained by separation of the variables. Such procedures were popular in the middle of the 20th century. The distributed resistance, F, may be written as

$$F = \frac{1}{2}\frac{c_f\rho|\vec{U}|}{D_h^2} \qquad [3]$$

where c_f is a non-dimensional friction coefficient,

$$c_f = \frac{\tau_w}{\frac{1}{2}\rho U^2} = \frac{a}{\mathrm{Re}} \qquad [4]$$

for fully-developed flow in ducts of constant cross-section (Poiseuille flow) and in the absence of mass transfer at the walls. τ_w may be regarded as an average shear stress $\tau_w = -\mu\overline{\partial u/\partial y}|_w$. However, more generally, it is to be considered an "effective" value[37] which lumps together both normal and shear forces and perhaps inertial effects as well (see below). The flow resistance is $FU = \tau_w B/A$, where A is the flow cross-sectional area, and B the thickness of the duct. Under the circumstance $c_f = c_f(x)$ and $\mathrm{Re} = \mathrm{Re}(x)$ are position-dependent, but $c_f\,\mathrm{Re}$ and F are not.

$$F = \frac{2a\mu}{D_h^2} \qquad [5]$$

where a is obtained from Shah and London,[37] for rectangular geometry, as

$$a = 24\left(1 + \sum_{n=1}^{n=5} a_n\alpha^n\right) \qquad [6]$$

where $\alpha = \max[B/H, H/B]$ is the channel aspect ratio, and a_n are empirical coefficients. For a square profile, Fig. 1, $B = H$, $\alpha = 1$, the hydraulic diameter (4 × Area/Perimeter), $D_h = 2H$ and $a = 14.2$, whereas for a plane duct, with boundaries at $y = \pm H$, Fig. 2a, $D_h = 4H$, $a = 24$ (Poiseuille formula).

The idea of a linear term in U for the hydraulic resistance, for laminar flow, and a quadratic term in U^2, for turbulent flow, was first proposed by Reynolds[9] in a study on boilers. He suggested that a similar term in the heat equation was also appropriate, see Beale[38] for a discussion and a simple empirical correlation that fits F to U in the laminar regime and to U^2 in the turbulent regime.

For multiply-connected regions, for example if the resistance were caused by fibers, e.g., in membrane spacers,[35] or offset fins, instead of a stack of plane ducts, then large-scale gradients in velocity, V, and pressure, P, would be present. This is also true in some fuel cell and electrolyzer designs, where serpentine and other complex macroscopic flow distributions may be encountered, and microscopic gradients are averaged-out.

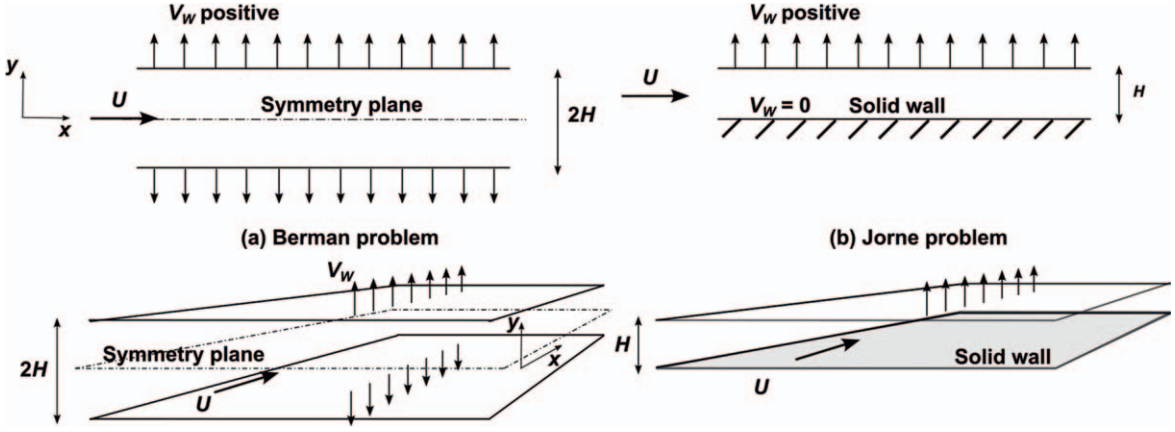

Figure 2. Geometry and boundary conditions for 2-D plane duct, illustrating the nomenclature. The width is presumed very large compared to the height, H. x is the streamwise and y the crosswise direction. (a) For Berman's problem[40] suction/injection occurs at both upper and lower boundaries corresponding to $y = \pm H$, whereas (b) Jorne[43] considered a similar problem but with mass transfer at only one boundary, e.g., at $y = +H$.

Here we consider flow in singly-connected regions associated with planar and rectangular ducts, so there are no large-scale lateral motions, V and W; only sub-scale components, v and w, associated with injection/suction at one or more walls are present. This simple analysis may then be extended to more complex shapes, such as serpentine passages.

Consider the case of a planar geometry with mass transfer at both boundaries separated by a distance $2H$, as shown in Fig. 2a. Note that here $D_h = 4H$. N.B.: This does not change Re which is based on D_h, only Re_W for which the characteristic length is H. Let it be supposed that the mixture density, ρ, and viscosity, μ, are the same for the injected/ejected fluid(s) and the mixture in the duct, and that these values are constant. With this, Eq. 2 takes the form

$$\rho U\frac{dU}{dx} = -\frac{dP}{dx} - FU \qquad [7]$$

The continuity equation may be written[d]:

$$\rho\frac{dU}{dx} = \dot{m}''' \qquad [8]$$

where, for constant wall velocity, $\dot{m}''' = \rho V_w/H$ or, in other words

$$\frac{dU}{dx} = \frac{V_w}{H} \qquad [9]$$

Integrating Eq. 7 and taking into account Eq. 8, the following form is obtained for the pressure change

$$\Delta P = -\left(F + \rho\frac{V_w}{H}\right)\left(U_0 + \frac{V_w}{2H}x\right)x \qquad [10]$$

Alternative form.—It is common to encounter expressions of the form

$$\vec{\nabla}P = -\hat{F}\vec{U}(x) \qquad [11]$$

in place of Eq. 2. The caret symbol is used to indicate that this resistance, $\hat{F}$, differs from the Patankar-Spalding resistance, F, given in Eq. 7 in that the inertial term is absent. Equation 2 may be considered, rather loosely, to be a specific instance of the Cauchy momentum equation, whereas Eq. 11 is an expression of static equilibrium. For cases where the inertial term in Eq. 7 is negligible, $d\vec{U}/dx = 0$, then Eq. 7 and Eq. 11 are identical with $F = \hat{F}$, otherwise from Eq. 10, for constant V_w,

$$\hat{F} = F + \rho\frac{V_w}{H} \qquad [12]$$

Reference to Eq. 12 will be made, below, when comparing the closed-form analytical expressions to the numerical CFD results based on the DRA.

Non-dimensional representation.—The term in the second parenthesis on the right-side of Eq. 10 is the mean local velocity, which for constant wall velocity may be written as

$$U(x) = U(0) + \frac{V_w x}{H} = U(0)\left[1 + 4\frac{\mathrm{Re}_W}{\mathrm{Re}(0)}\frac{x}{H}\right] \qquad [13]$$

where

$$\mathrm{Re}_W = \frac{\rho V_w H}{\mu} \qquad [14]$$

is the wall Reynolds number.[e]

$$\mathrm{Re}(x) = \frac{\rho U(x) D_h}{\mu} = 4\frac{\rho U(x) H}{\mu} \qquad [15]$$

is the flow Reynolds number at x. From Eq. 13 the local Reynolds number may be written

$$\mathrm{Re}(x) = \mathrm{Re}(0)\left(1 + 4\frac{\mathrm{Re}_W}{\mathrm{Re}(0)}\frac{x}{H}\right) \qquad [16]$$

Equation 4 with Eq. 16 gives the form for the friction coefficient that was given in Beale.[32] In anticipation of the Berman analysis,[40] below, it is assumed that to first order

$$c_f(x) = \frac{a(1 + b\mathrm{Re}_W)}{\mathrm{Re}(x)} \qquad [17]$$

and

$$c_f^*(x) = \frac{a}{\mathrm{Re}(x)} \qquad [18]$$

c_f is the friction coefficient. Consistent with the mechanical engineering mass transfer literature notation,[41,42] the asterisk denotes "for zero net mass flux through the wall" (The reader who has difficulty with this concept should consider the case of the chemical catalytic reactor where there is no net mass transfer at the boundary, though there are gradients in individual species.) Equation 18 is the form associated with the Poiseuille equation in elementary fluid mechanics. Adopting similar notation for the distributed resistance,

$$F = \frac{2a\mu(1 + b\,\mathrm{Re}_W)}{D_h^2} \qquad [19]$$

$$F^* = \frac{2a\mu}{D_h^2} \qquad [20]$$

and

$$F/F^* = 1 + b\mathrm{Re}_W \qquad [21]$$

Equations 19 and 21 are the required prototypes for investigating the influence of boundary and inertial effects on the basic form, Eq. 20. As will be shown below, the additional b-term includes mass transfer effects due to both changes in wall shear stress (boundary effects) and also to mass being added or removed (inertial effects). Since Re_W magnitudes are generally small for electrochemical reactions, higher order terms in the series expansion $F/F^* = 1 + b\mathrm{Re}_W + c\mathrm{Re}_W^2 + \ldots$ are negligible for the present application.

Analytical Solution for the Micro-scale Problem with Constant Wall Velocity

In Berman's work[40] on reverse osmosis, both V_w and Re_W were considered positive for suction, negative for injection. This is the opposite of the usual convention in heat and mass transfer texts. Since there is a large volume of literature surrounding Berman's work, following the former convention; in this section alone, the notation follows that of Berman. For the remainder of the paper, however, the notation reverts to the more usual positive-injection, negative-suction rule, changing the sign of odd terms in Re_W, in

[d]The notation follows that of Jacob,[39] whereby a "dot" denotes per unit time and a "dash" per unit length, so that if m is mass in kg, then $\dot{m}''$ is mass flux in $\mathrm{kg}\cdot\mathrm{m}^{-2}\cdot\mathrm{s}^{-1}$ and $\dot{m}'''$ is in $\mathrm{kg}\cdot\mathrm{m}^{-3}\cdot\mathrm{s}^{-1}$. In this paper, a "dash" is never used to denote an ordinary derivative.

[e]N.B.: There is no logical reason for basing Re_W on H. It would be less confusing if it were based on D_h, as is the main flow Reynolds number, Re. Reluctantly, the authors bow to convention on this subject.

particular that of the linear b-term in Eq. 19. It is hoped that this does not create any confusion for the reader. The Jorne analysis[43] was similar to that of Berman,[40] but based on a single rather than a pair of permeable boundary planes, Fig. 2b. The latter approximates more closely the situation in present-day fuel cells and electrolyzers whereas the former resembles the situation in many membrane filtration systems. In both cases, the constant property Navier-Stokes equations

$$\rho\frac{\partial\vec{u}}{\partial t} + \rho\vec{u}\cdot\vec{\nabla}\vec{u} = -\vec{\nabla}p + \mu\nabla^2\vec{u} \qquad [22]$$

were considered. For 2-D flow, a stream function, ψ, may be expressed as

$$\psi = [HU(0) - V_w x]f(\tilde{y}) \qquad [23]$$

where $\tilde{y} = y/H$ is a non-dimensionalized coordinate. An approximate solution, valid for small Re_W based on a linear perturbation type analysis can be derived.[40] From Berman's analysis it follows that the pressure equation may be conveniently written,

$$\frac{dp}{dx} = k\frac{\mu}{H^2}\left(U(0) - \frac{V_w x}{H}\right) \qquad [24]$$

where

$$k = \mathrm{Re}_W(f^{(1)}f^{(1)} - ff^{(2)}) + f^{(3)} \qquad [25]$$

and $f^{(n)} = \partial^n f/\partial\tilde{y}^n$. The reader will note that $dk/dy = 0$, so that

$$\mathrm{Re}_W(f^{(1)}f^{(2)} - ff^{(3)}) + f^{(4)} = 0 \qquad [26]$$

Asymptotic solution to Eq. 25 for $\mathrm{Re}_W << 1$ subject to the given boundary conditions leads to the solution for the f-function[40,43] as follows;

$$f(\tilde{y}) = \frac{\tilde{y}(3-\tilde{y}^2)}{2} + \mathrm{Re}_W\frac{-\tilde{y}^7 + 3\tilde{y}^3 - 2\tilde{y}}{280} \quad \text{Berman} \qquad [27]$$

$$f(\tilde{y}) = -2\tilde{y}^3 + 3\tilde{y}^2 + \mathrm{Re}_W\frac{-16\tilde{y}^7 + 56\tilde{y}^6 - 84\tilde{y}^5 + 108\tilde{y}^3 - 64\tilde{y}^2}{280} \quad \text{Jorne} \qquad [28]$$

for the cases shown in Figs. 2a, 2b. The resistance, including inertial and viscous effects may be written,

$$\hat{F} = \frac{\bar{k}\mu}{H^2} = \frac{\mu}{H^2}[\mathrm{Re}_W(\overline{f^{(1)}f^{(1)}} - \overline{ff^{(2)}}) + \overline{f^{(3)}}] \qquad [29]$$

The individual components due to streamwise and streamwise inertia and viscous resistance are tabulated in Table I. The reader will note that while $\bar{k} = k$ is independent of $\tilde{y}$, that is not true for the components, $\overline{f^{(1)}f^{(1)}} \neq \overline{f^{(1)}}\cdot\overline{f^{(1)}}$ etc... In other words $\overline{UU} \neq \overline{U}\cdot\overline{U}$. This has implications for the inertial terms, discussed further below.

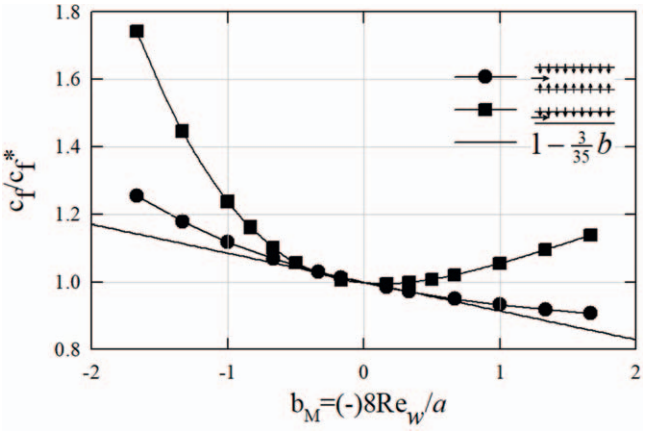

Figure 3. Normalized friction coefficient from Beale[32] (modified). The Berman solution[40] is shown as a straight line, and CFD results as circles and squares. The non-dimensional blowing parameter, b_M, is negative for suction and positive for injection, i.e., opposite to Re_W as defined by Berman.[40,43] Reproduced with the permission of the National Research Council of Canada, copyright holder.

Viscous boundary effects only.—Consider only the viscous contribution, $-\mu\overline{f^{(3)}}/H^2$, neglecting inertial effects in Eq. 29

$$\hat{F} = \frac{\mu}{H^2}\left(3 + \frac{3}{35}\mathrm{Re}_W\right) = \frac{48\mu}{D_h^2}\left(1 + \frac{1}{35}\mathrm{Re}_W\right) \quad \text{Berman} \qquad [30]$$

$$\hat{F} = \frac{\mu}{H^2}\left(12 + \frac{3}{35}\mathrm{Re}_W\right) = \frac{48\mu}{D_h^2}\left(1 + \frac{1}{140}\mathrm{Re}_W\right) \quad \text{Jorne} \qquad [31]$$

It is seen that suction, which corresponds to a positive Re_w in Berman's notation, increases friction and therefore the overall resistance to flow. This is because the value of the tangent dU/dy (the slope of the parabola) and therefore the magnitude of the shear stress, τ_w, increases for suction and decreases for injection. Therefore, at a given streamwise velocity, U, the magnitude of the streamwise pressure gradient decreases for injection and increases for suction. Figure 3 shows calculations performed using the CFD code PHOENICS[32] (**P**arabolic **H**yperbolic **O**r **E**lliptic **N**umerical **C**ode **S**eries). The shear stress, $\tau_w = \mu\partial u/\partial y$, is calculated from the velocity gradient (tangent) at the boundary wall. Equations 30-31 correspond to tangents to the plane duct solution at $\mathrm{Re}_W = 0$. This is because the Berman/Jorne solution is based on the application of small perturbation around the Poiseuille solution, $V_w = 0 \pm \delta$. It can be seen that as the magnitude of Re_w, or equivalently the blowing parameter b_M, increases, the numerical values depart increasingly from the linear (in Re_w) Berman solution.

Table I. Inertial and viscous terms as a function of the $f(\tilde{y})$ and its derivatives, integrated across the flow in the $\tilde{y}$ direction. Overbars denote averaged values.

		Berman[40]	Jorne[43]
Streamwise inertia	$\overline{f^{(1)}f^{(1)}}\,\mathrm{Re}_W$	$6\mathrm{Re}_W/5 - 2\mathrm{Re}_W^2/525 + \ldots$	$6\mathrm{Re}_W/5 - \mathrm{Re}_W^2/1050 + \ldots$
Crosswise inertia	$\overline{ff^{(2)}}\,\mathrm{Re}_W$	$-6\mathrm{Re}_W/5 + 2\mathrm{Re}_W^2/525 + \ldots$	$-6\mathrm{Re}_W/5 + \mathrm{Re}_W^2/1050 + \ldots$
Crosswise viscous	$\overline{f^{(3)}}$	$-3 - 3\mathrm{Re}_W/35 + \ldots$	$-12 - 3\mathrm{Re}_W/35 + \ldots$
Total	$\bar{k}$	$-3 + 81\mathrm{Re}_W/35 + \ldots$	$-12 + 81\mathrm{Re}_W/35 + \ldots$

The reader may question the reason for the author's introduction of b_M, as independent variable, rather than Re_W. This stems from mass transfer theory[41,42] where the normalized Sherwood number, Sh/Sh* (or g/g^*) is frequently plotted against scalar mass transfer blowing parameter, $b_M = \dot{m}''/g^*$, and g^* and Sh* are the conductance or mass transfer coefficient and Sherwood number in the limit $\dot{m}'' \to 0$. The blowing parameter, b_M, thus represents the ratio of convection to diffusion, i.e., the mass transfer Péclet number. By analogy[41] between the friction coefficient, $2c_f^* = \tau_w/(\rho UU)$ and the Stanton number for mass transfer, $St = Sh/(Re{\cdot}Sc) = J/(\rho U)$, the momentum blowing parameter, $b_M = 2V_w/(Uc_f^*) = \pm 8Re_W/a$ (minus for Berman's definition of V_w/Re_W above, or plus as defined elsewhere), is thus suitable for comparison of momentum transfer with mass transfer results.[32] The reader may prefer to simply consider the abscissa in Fig. 3 as being proportional to the wall Reynolds number, Re_W. It can be seen that for both the Berman[40] and Jorne[43] problems, c_f increases for suction. For mass transfer at both walls,[40] c_f decreases for injection, whereas for mass transfer at only one wall,[43] it initially decreases but then increases. The distribution for rectangular ducts displays substantially larger changes in c_f as a function of injection/suction, compared to the results for plane ducts.[32]

Sample calculations for a PEMFC, below, show that a typical value of b_M is 0.0174, corresponding to a very small $Re_w = 0.0522$, implying that not only are departures from the linear solution very small, but also $c_f/c_f^* \approx 1$ i.e., the Poiseuille equation is a very good approximation for the streamwise flow velocity and the linear term in Eq. 17 is very small or redundant.

Combined microscopic inertial and viscous effects.—If both inertial components and viscous effects are included in the calculation then

$$\hat{F} = \frac{\mu}{H^2}\left(3 - \frac{81}{35}Re_W\right) = \frac{2\mu}{D_h^2}\left(24 - \frac{648}{35}Re_W\right) \quad \text{Berman} \quad [32]$$

$$\hat{F} = \frac{\mu}{H^2}\left(12 - \frac{81}{35}Re_W\right) = \frac{2\mu}{D_h^2}\left(24 - \frac{162}{35}Re_W\right) \quad \text{Jorne} \quad [33]$$

Thus the change in pressure is given by

$$\Delta p = -\hat{F}\left(U(0) + \frac{V_w x}{2H}\right)x \quad [34]$$

Inertia has the opposing tendency to friction; suction decreases the resistance due to the "Bernoulli effect": in the absence of viscous drag, for ideal flow, i.e., $\mu = 0$ in Eq. 22 for plug flow, then $p + \frac{1}{2}\rho|\vec{u}^2| = \text{constant}$, $dp/dx > 0$ for suction and $dp/dx < 0$ for injection (or alternatively set $F = 0$ in Eq. 2 with $P + \frac{1}{2}\rho|\vec{U}|^2 = \text{constant}$). Since the effect of viscous drag is always a pressure decrease, $dp/dx < 0$, the impact of inertia is to increase the magnitude of the pressure gradient for injection, and decrease it for suction. This effect was previously observed in the manifolds of industrial solid oxide fuel cell stacks.[44]

Macroscopic streamwise inertia.—Although Eq. 32 appears suitable for direct substitution into Eq. 7: Equation 7 already contains a macroscopic inertial term, $\rho UdU/dx$, which appears as V_w/H in Eq. 10. No such inertial term is present in Eq. 34. Therefore to avoid "double counting" set, F, as distinct from $\hat{F}$, according to Eq. 12, $F = \hat{F} - \mu Re_W/H^2$, so that

$$F = \frac{\mu}{H^2}\left(3 - \frac{46}{35}Re_W\right) = \frac{48\mu}{D_h^2}\left(1 - \frac{46}{105}Re_W\right) \quad \text{Berman} \quad [35]$$

Table II. Dimensions and other parameters employed for the baseline case. Incompressible flow in a polymer electrolyte membrane fuel cell cathode. Based on the example in Kulikovsky.[45]

Channel length, L	m	1.0
Channel height, H	m	5×10^{-4}
Air flow stoichiometry, λ		1.5
Inlet pressure, $P(0)$	bar	1
Cell temperature, T	K	353
Inlet oxygen mole fraction, X_{O_2}		0.21
Inlet velocity, $U(0)$	$m{\cdot}s^{-1}$	10.864
Wall velocity, V_w	$m{\cdot}s^{-1}$	1.9692×10^{-3}
Wall mass flux, $\dot{m}''$	$kg{\cdot}m^{-2}\cdot s^{-1}$	1.9692×10^{-3}
Current density, j''	$A{\cdot}m^{-2}$	10 000
Reynolds number, Re_{D_h}/Re_H		576/144
Wall Reynolds number, Re_W		0.0522
Molar mass, $M_i[H_2O, O_2, N_2]$	$kg{\cdot}mol^{-1}$	$[18, 32, 28]\times10^{-3}$
Air density, ρ	$kg{\cdot}m^{-3}$	1.00*
Air kinematic viscosity, ν	$m^2\cdot s^{-1}$	1.886×10^{-5}
Water transfer coefficient, n_d		1

$$F = \frac{\mu}{H^2}\left(12 - \frac{46}{35}Re_W\right) = \frac{48\mu}{D_h^2}\left(1 - \frac{23}{210}Re_W\right) \quad \text{Jorne} \quad [36]$$

Thus, when employing CFD with the DRA approach, Eqs. 35–36 are the preferred forms for F, whereas when the direct analytical solution to the Berman/Jorne problem is required for verification, Eqs. 32–34 are employed. When the Poiseuille solution is employed for the resistance, $\hat{F} = 48D_h^2/\mu$, no such distinction is required, $F^* = \hat{F}^*$.

Computational Fluid Dynamics

Henceforth the convention that velocity is positive for injection, and negative for suction, is adopted for the remainder of the text. Thus for Berman's problem; Eq. 35 may be written in terms of Eq. 19, with $a = 24$ and $b = +46/105$; and Jorne's problem, Eq. 36 with $a = 24$ and $b = +23/210$ (note sign changes). Using these values the pressure is calculated using Eq. 10. Also the blowing parameter in Fig. 3 is $b_M = +8Re_W/a$.

In this section, sets of calculations based on; (i) detailed CFD DNM calculations, and (ii) CFD calculations based on the DRA approach, are compared with each other, and with the theoretical Berman/Jorne formulation. In all cases, calculations were performed using the the numerical integration code library/series, `OpenFOAM` (Open source **F**ield **O**peration **A**nd **M**anipulation).

Sample problem.—The problem considered is the cathode of an idealized polymer electrolyte membrane fuel cell with hydrogen as fuel. Table II lists values, assuming constant properties similar to those given by Kulikovsky,[45] which is for the air electrode of a PEMFC. (Kulikovsky used $\rho = 1.06 kg\cdot m^{-3}$ whereas here $\rho = 1.00 kg\cdot m^{-3}$, for air). In a PEMFC cathode, protons combine with oxygen and electrons to produce water. In crossing the membrane from the anode to the cathode, the H^+ protons drag water molecules with them. The mass flux at the wall, corresponding to the electrode is therefore given by,

$$\dot{m}'' = \frac{1}{4F_c}[2(1 + 2n_D)M_{H_2O} - M_{O_2}]j'' \quad [37]$$

where F_c is Faraday's constant, n_D is the osmotic drag cofficient, M_{H_2O} and M_{O_2} are the molar masses of water and oxygen, and j'' is the current density.

The wall velocity is just

$$V_w = \frac{\dot{m}''}{\rho} \qquad [38]$$

In a PEMFC, the inlet velocity, $U(0)$, is normally adjusted to produce a fixed stoichiometry number, λ, that is the ratio of the total available flux of oxidant to the amount consumed by the reaction (the inverse of the so-called utilization), in other words

$$U(0) = \lambda \frac{j'' L}{4 \mathrm{F_c} X_{\mathrm{O_2}} c_{\mathrm{air}} H} = \lambda \frac{\mathrm{M_{O_2}} j'' L}{4 \mathrm{F_c} Y_{\mathrm{O_2}} \rho_{\mathrm{air}} H} \qquad [39]$$

where H is the channel height, $X_{\mathrm{O_2}}$ and c_{air} are the oxygen mole fraction and air concentration at the inlet, $c_{\mathrm{air}} = P/RT$. Alternatively $Y_{\mathrm{O_2}}$ is mass fraction and $\rho_{\mathrm{air}} = M_{\mathrm{air}} c_{\mathrm{air}}$ is mixture density, and $M_{\mathrm{air}} = \Sigma X_j M_j$ is the mixture molar mass of the air. It can be seen from Table II that the value of Re_W and hence the blowing parameter $\mathrm{b_M}$ is very small, so that $c_f/c_f^* \approx 1$.

Micro-scale detailed numerical model (DNM).—A rectilinear mesh of size 100×40×1 was constructed. For Berman's problem, due to symmetry, only one half of the y-domain was considered, $0 \leqslant y \leqslant H$ in Fig. 2, and the mesh was concentrated toward the wall away from the symmetry plane. The inlet streamwise and crosswise velocity were prescribed according to the simplified equations given in Eqs. A.4 and A.5 in Beale.[32]

For Jorne's problem, the mesh was concentrated toward both walls, and no slip $\vec{u} = \vec{0}$ was prescribed at the alternate boundary. In both cases, at the porous wall the boundary velocity was prescribed as $\vec{u} = (0, V_w, 0)$. The downstream gauge pressure (i.e., pressure relative to 1 atm) was fixed to a value of zero.

Figure 4 is a comparison of the results calculated using Berman's solution, Eqs. 32 and 34, with the detailed micro-scale CFD simulation. It can be seen that agreement is near perfect. The streamwise coordinate (along the channel) has been non-dimensionalised as $\tilde{x} = x/L$ and pressure as $\tilde{p} = (p - p(L))/\frac{1}{2}\rho U(0)^2$, sometimes referred to in the literature as an Euler number. Inlet and wall velocities are indicated in Table II corresponding to a stoichiometric number, $\lambda = 1.5$, and fixed current density, $j'' = 10000$ A m^{-2} similar to those prescribed by Kulikovsky.[45] Also shown is the profile for $V_w = 0$ based on the well-known analytical solution for Poiseuille flow. It can be reasonably concluded from this figure, that the DNM CFD model is in good agreement with the Berman solution and may therefore be reliably used for comparison with the DRA method, as described below.

Figure 5 is a comparison of Jorne's solution, Eqs. 33 and 34, in terms of $\tilde{p}$ versus $\tilde{x}$ for a similar case. It can be seen that, once again, the agreement between the DNM and analytical solutions is near perfect. The overall pressure losses are of the order of 4 × (four times) those displayed in Fig. 4 as the hydraulic diameter is 2 × larger in the former case, thereby decreasing the pressure by a factor of 4. Consistent with the results of Kulikovsky,[45] the Poiseuille solution pressure distributions in Figs. 4–5 are seen to deviate significantly from the Berman/Jorne results, as well as the corresponding CFD/DNM calculations. Henceforth, in this work, the Jorne solution will be considered exclusively, since it is closer to the physical situation in fuel cells and electrolyzers than is that of Berman.

Macro–scale distributed resistance analysis (DRA).—The DRA model was based on a simplified version of an existing implementation designed to perform fuel cell calculations. The distributed resistance, F, is introduced by means of a volumetric source term, and slip boundaries are presumed at the side(s). Given the simplifications of the present study, the implementation of the DRA in `OpenFOAM` requires less effort here than for more complex/realistic situations, where variations in temperature, density, species concentrations, etc... must be taken into account.[11–13] The existing modules in `OpenFOAM` offer the possibility to achieve the goal without need for significant programming. The authors employ `porousSimpleFoam`, with the mass source/sink in the continuity equation, $\dot{m}'''/\rho = V_w/H$, prescribed in the input file `transportProperties`, and the momentum sink term as a so-

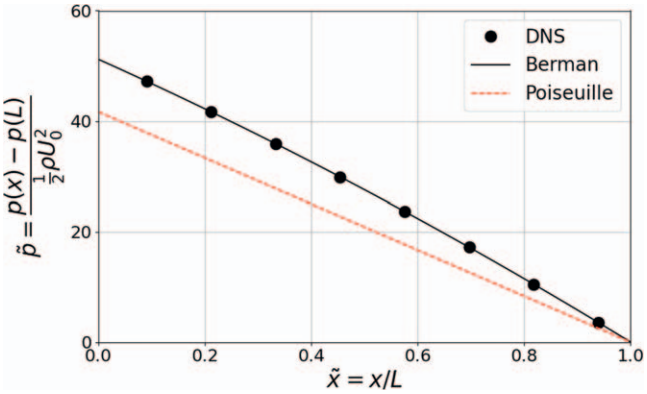

Figure 4. Comparison of the analytical solution of Berman, as given in Eqs. 32 and 34 with micro-scale DNM calculation for a PEMFC channel, constant current density, $j'' = 1 \cdot 10^4$ A m^{-2}, and the Poiseuille solution for $j'' = 0$ A m^{-2}.

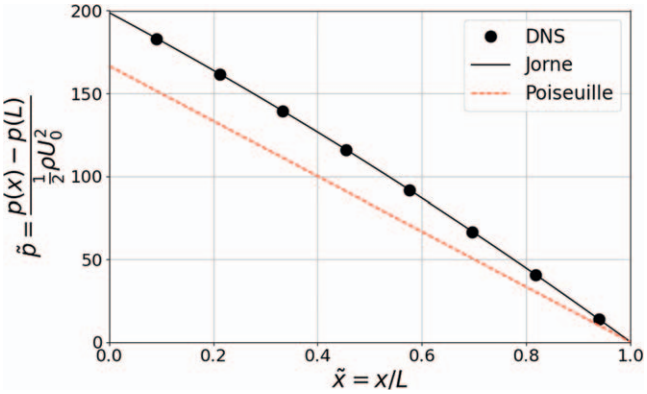

Figure 5. Comparison of the analytical solution of Jorne, as given in Eqs. 33 and 34 with micro-scale DNM calculation for a PEMFC channel, constant current density, $j'' = 1 \cdot 10^4$ A m^{-2}, and the Poiseuille solution for $j'' = 0$ A m^{-2}.

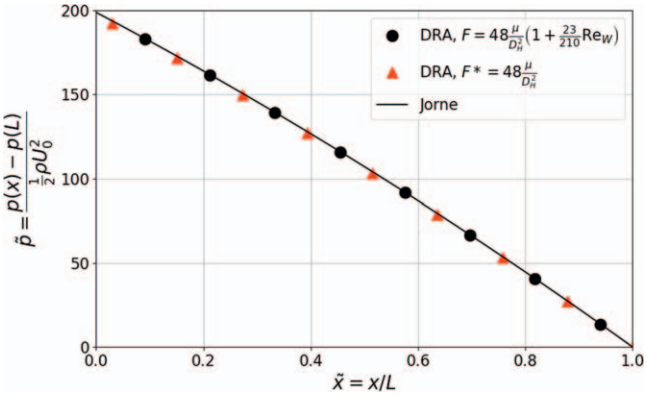

Figure 6. Comparison of the analytical solution of Jorne, as given in Eqs. 33 and 34 with DRA calculations, or a PEMFC channel, constant current density, $j'' = 1 \cdot 10^4 \mathrm{Am}^{-2}$.

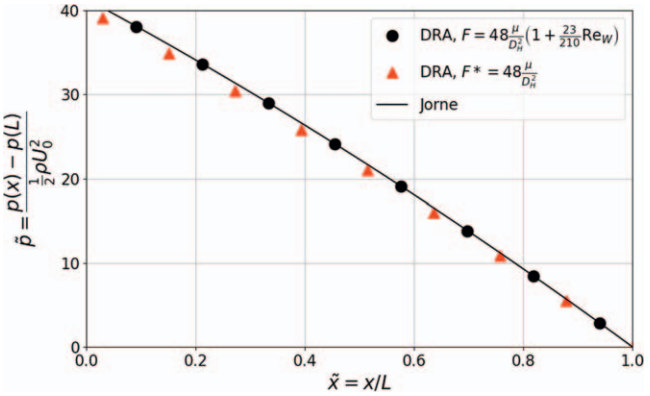

Figure 7. Comparison of the analytical solution of Jorne, as given in Eqs. 33 and 34 with DRA calculations, or a PEMFC channel, constant current density, $j'' = 5 \cdot 10^4 \mathrm{Am}^{-2}$.

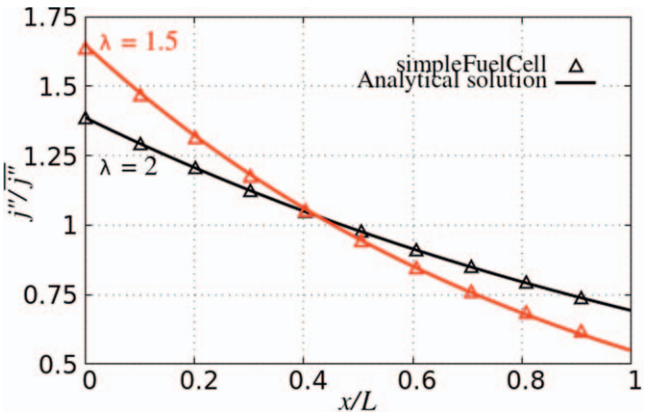

Figure 8. Effects of stoichiometric number, λ, on normalized local current density, $j''/\overline{j''}$, for a first-order reaction. Comparison of the analytical expression Eq. 42, Kulikovsky et al.,[46,47] with numerical results from the CFD code, `simpleFuelCell`. For further details see Beale.[48]

called "Darcy" resistance, $d = F/\mu$ in `porosityProperties` file, both these files are located in the `constant` directory for the case-at-hand. (The associated "Forchheimer" term is set to zero, $f = 0$, in `porosityProperties`.)

Constant current density.—Figure 6 is a comparison of the results calculated using Jorne's solution, Eqs. 32–34 with the DRA calculations, Eq. 35, for the same case as shown in Fig. 5 based on the DNM approach corresponding to $j'' = 10^4$ A m^{-2}. It can be seen that when the resistance is based on the zero-wall velocity value F^*, Eq. 20, as commonly employed in the past, the pressure gradient is close to the theoretically-derived value, but slightly lower. The reader will note that although F^* is based on the Poiseuille equation, $F^* = 48\mu/D_h^2$, in this case the bulk velocity $U = U(x)$ is varying due to continuity. Therefore the deviation from the analytical solution of Berman is relatively small in comparison to Fig. 4. When the viscous and inertial corrections are introduced in the form of Eq. 35, agreement with the analytical Berman solution, (and the detailed CFD results, not shown) is near-perfect.

The results shown in Fig. 7 differ from those in Fig. 6 due to the fact that the current density is increased to $j'' = 5 \cdot 10^4$ A m^{-2}, again for $\lambda = 1.5$. It can be seen that as Re_W increases five-fold over the base case, calculations based on F^* start to deviate a little from the analytical values and those based on F. However the deviation is not very large. Only for large values of Re_W are boundary and inertial effects of any consequence, provided the local velocity, $U(x)$ not $U(0)$, is used in the calculation of $F^* = a/\mathrm{Re}_W$.

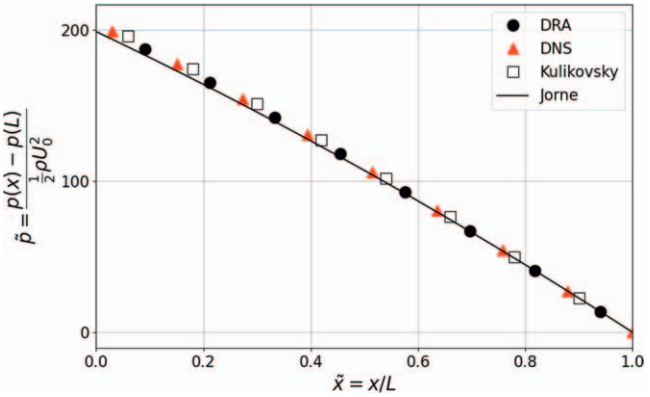

Figure 9. Normalized pressure distribution, variable current density, $j'' = 10^4$ A m^{-2}, $\lambda = 1.5$.

Variable current density.—Up to now, the results have all presumed constant current density. Although uniform current density is a desirable feature for electrochemical cells, it is never attained in practice. In this Section a comparison is made between the DRA and the numerical approach of Kulikovsky,[45] for variable current density, $j''(x)$. Under the circumstances, Eq. 26 contains additional terms with the derivatives of $\tilde{V}_w$ with respect to $\tilde{x}$; $\tilde{V}_w^{(1)}$, $\tilde{V}_w^{(2)}$, $\tilde{V}_w^{(3)}$:

$$\begin{aligned}&(1 + \mathcal{R})\tilde{V}_w(f^{(1)}f^{(2)} - ff^{(3)})\\ &-(\tilde{V}_w\tilde{V}_w^{(1)} - (1 + \mathcal{R})\tilde{V}_w^{(2)})ff^{(1)}\\ &= \tfrac{1}{\mathrm{Re}_w}((1 + \mathcal{R})f^{(4)} + \tilde{V}_w^{(3)}f + 2\tilde{V}_w^{(1)}f^{(2)}).\end{aligned} \quad [40]$$

However a numerical solution of the ordinary differential equation, Eq. 40, is still possible. Here, $\tilde{V}_w = V_w/U_0$ and

$$\mathcal{R} = \frac{L}{H}\int_0^{\tilde{x}} \tilde{V}_w \, d\tilde{x} \quad [41]$$

where $\tilde{x} = x/L$. Kulikovsky and co-workers[46,47] previously obtained expressions for the local current density in 1-D: Assuming, say, the kinetics of the oxygen reduction reaction may be described in terms of a first-order Tafel expression, together with a number of other simplifications, the following expression was derived;

$$\frac{j''}{\overline{j''}} = -\lambda \ln\left(1 - \frac{1}{\lambda}\right)\left(1 - \frac{1}{\lambda}\right)^{\tilde{x}} \quad [42]$$

$$\frac{V_w(x)}{V_w(0)} = \left(1 - \frac{1}{\lambda}\right)^{\tilde{x}} \quad [43]$$

where $\overline{j''}$ is the mean value of j''. The book chapter by Beale[48] lists the assumptions inherent in the derivation of Eq. 42, and compares both the current density distribution, $j''/\overline{j''}$, and the oxygen concentration/mass fraction distributions, with detailed CFD work, obtained using a simple open-source educational code, `simpleFuelCell`. Figure 8 shows the effect of λ on the current density. Note that both the variance in the current density and the non-linearity in the distribution increase as λ decreases. Values of λ smaller than 1.25 are seldom realized in practical electrochemical devices.

Figure 9 shows the pressure distribution for applied current density/wall velocity computed according to Eqs. 42, 43. It can be seen that solution to Eq. 40 (variable V_w) deviates only slightly from the curve for the constant V_w case. Further, agreement between the "exact" DNM solution and the volume-averaged DRA method is excellent, giving further credence as to the validity of the DRA model for the case of variable current density.

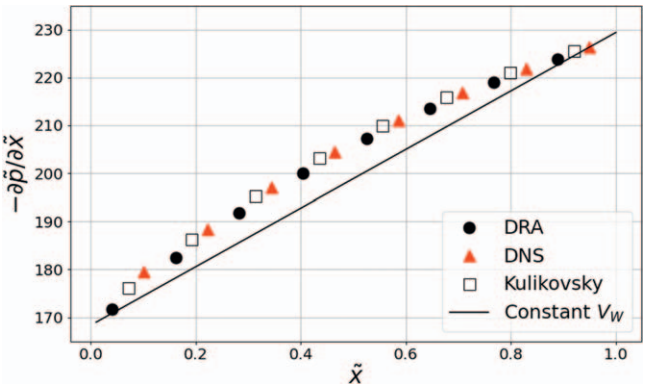

Figure 10. Normalized pressure gradient along channel centerline, variable current density, $j'' = 10^4$ A m^{-2}, $\lambda = 1.5$.

Figure 10 shows the centerline pressure gradient, normalized for the DNM and DRA cases compared to the numerical solution of Kulikovsky. Also shown is the numerical solution for constant current, corresponding to Jorne's solution. Pressure gradient is thus seen to be more sensitive to the choice of velocity boundary condition than is pressure. There is excellent agreement between the results of the DRA, DNM and Eq. 40 in terms of $\partial\tilde{p}/\partial\tilde{x}$ with the constant value underpredicting the case of variable current density.

The fluid motion in the channel is coupled to the distribution of the local current density. Numerical examples in Figs. 9, 10 should be considered as zero-order approximations. The first-order correction to the local current distribution could be obtained by using the zero-order flow velocity and pressure distributions. If necessary, this iterative process can be continued. However, the largest contribution usually give the zero-order shapes, which are presented in Figs. 9, 10.

Discussion

The results show that by-and-large, the DRA approach of Patankar and Spalding[1] generate meaningful results when compared to the analytical theory of Berman and Jorne[40,43,49] for constant current density and with the recent work of Kulikovsky[45] for variable current density. It is shown that under the circumstances the simplified form for the resistance, based on the zero-mass transfer approximation, F^*, Eq. 20, generates sufficiently accurate results in terms of predicted pressure losses: By including a linear term in V_w for F, Eq. 19, only slightly better agreement with analytical solutions based on perturbation theory are obtained. This is due to the wall Reynolds numbers being small for the problem at hand; should these increase, boundary layer and inertial effects would become significant, as noted in Kulikovsky.[45] In microchannels, where h is an order of magnitude lower and in filtration applications, where the absolute value of V_w could be much larger, the effects will be large. The present results may appear, superficially, to be at odds with those of ref.[45], where significant differences in the solution for pressure gradient were noted for (constant and variable) Berman and Poiseuille formulae, over the length, L. However, the DRA approach is based on a finite-volume numerical integration procedure, and the pressure gradient is therefore approximated by a "staircase" series of values at each computational cell, length Δx, and thereby F continuously adjusted for variable local in-cell velocity over length, L. It is for this reason that values of $\tilde{p}$ with F based on local value of $U(x)$ are in good agreement, as compared to those shown in Figs. 4 and 5.

For the problems-at-hand, the contributions due to streamwise and crosswise inertia are numerically equal. Axial viscous diffusion in the streamwise direction is generally-speaking very small; vanishingly small in both Berman and Jorne's analyses where, because of the definition of the 2-D stream function Eq. 23, $\partial^2 u/\partial x^2 = 0$. Note that for more complex flow geometries, profile drag can also contribute to F, in addition to shear stresses.

The closed-form solutions are for constant density and viscosity. Variations in transport properties are readily accounted-for in both the DRA (Nishida et al.[50]) and DNM (Beale et al.[51]) In addition to the continuity and momentum equations, an equation-of-state is required to obtain local values of partial density, for instance, $\rho_i = px_iM_i/RT$ (DNM) or PX_iM_i/RT (DRA), where x_i or X_i, is the molar fraction of species i, molar mass M_i. The mixture density is just the arithmetic sum of the partial densities of reactants, products, and inert species, $\rho = \sum_{i=1}^{n} \rho_i$, in each computational cell. These require the solution of mass balance equations for individual species, based on Maxwell-Stefan or Fick's law (DNM), or alternatively a mass transfer conductance (DRA). Individual and overall species sources/sinks are computed according to Faraday's law of electrolysis. Solution to an energy conservation equation is also required, if temperature variations are significant. The individual gas component viscosities may be obtained as a function of temperature and pressure, $\mu_i(p, T)$, see Poling et al.[52] These are then combined to obtain a local mixture viscosity, Wilke.[53] The effect of variable fluid properties (viscosity, conductivity, specific heat) in SOFCs is discussed in Nishida et al.[50]

The reader will note that property variations for two-phase (liquid-gas) flow are very large. These have been addressed in some stack models,[14] using an Euler-Euler two-fluid approach. Substantial savings can be made if a pseudo-single phase model is employed in the channels (algebraic slip, or drift flux[54]) and the porous layers[55] (mixture). There is scope for additional research here. Although, the calculations presented here were for an idealized PEM fuel cell; the analysis is equally valid for electrolyzers.

It was shown that differences in pressure were due to (i) shear terms associated with changes in the velocity gradient angle/tangent at the wall and (ii) changes in the velocity profile on a microscopic scale. For the latter, it is to be noted that the macroscopic inertia term on the left-hand side of Eq. 2 is only approximate other than for ideal or plug flow: For the Berman solution it is seen that $\overline{UU} = 6\overline{U}^2/5$, whereas for a square profile one would expect $\overline{UU} \simeq 36\overline{U}^2/25$. For more complex geometries (non-rectangular cross-sections etc...) should a b-term be required for F, Eq. 19, analytical solutions may not be readily available and F can best be calculated by performing detailed micro-scale simulations (also true for the a-term), by varying the Re_W.

One might speculate under what circumstance the macroscopic inertial term on the left-side of Eq. 2 can be neglected. There are a number of situations, apart from constant property, fully-developed duct flows, where the "Darcy's law" form Eq. 11 may be employed, especially for low Reynolds numbers flows. However there are also numerous applications where inertia is significant: Consider for example, ducts with inserts to promote mixing, electrical conduction, or mechanical stability, e.g., in solid oxide fuel cells and membrane filtration systems. It is therefore prudent to retain inertial (and where necessary transient) terms for a general formulation. Analytical solutions[40,43] for plane ducts provide useful benchmarks for constant density and wall velocity. However, the distributed resistance method may readily be employed for rectangular or other cross-section ducts, not necessarily straight (curved or serpentine) channels, with variable wall velocity, density etc., more typical of practical electrochemical devices. It therefore represents a powerful methodology based on sound principles, with widespread application.

This paper was concerned with generation of canonical examples to assess the accuracy of pressure predictions using a distributed resistance analogy, based on Reynolds' concept of flow resistance, which has proved to be a useful predictor for hydraulic performance in fuel cells and electrolyzer stacks and many other applications. In this work, attention was focused exclusively on hydraulic resistance, i.e., pressure losses. The important subject of validation and verification and the reliability of the methodology for heat and mass transfer may also be considered in the context of analytical and semi-numerical solutions, for example the work of Sherwood et al.,[56,57] in a future analysis.

Chelham et al.[58] provide a comprehensive review of flow in porous ducts The authors note that; in contrast to theoretical and

numerical work, relatively few experimental investigations have been undertaken with regard to velocity profiles, pressure distributions, and friction factors. Nevertheless, Gupta and Levy[59] observed good agreement between experimental data on pressure drop and similarity solutions with uniform injection. Suction solutions were, however, found to be accurate only for small values of Re_W. Beavers et al.[60] considered experiments with a rectangular duct bounded by a porous transport layer, with associated tangential slip velocity, dependent upon permeability, with only axial flow (i.e., no injection/suction); a refinement potentially worth incorporating in future detailed work involving porous transport/gas diffusion layers.

Conclusion

The distributed resistance analogy can accurately replicate detailed numerical simulations and analytical solutions based on planar geometry for both constant and variable current density. Microscopic boundary and inertial effects, associated with the change in velocity profile tangent, and added/removed mass, do not alter the solution in a significant way, at least for the magnitude of current densities encountered in present-day electrochemical devices, such as fuel cells and electrolyzers. The main influence of macroscopic inertia (changes in $U(x)$) is to proportionally increase or decrease the flow resistance, F. For this reason F must always be calculated, based on the local velocity, $U(x)$, not the inlet $U(0)$, or some other constant value. Employing the zero-mass transfer resistance, F^*, in place of F, under these circumstances will render sufficiently accurate solutions for the pressure gradient under normal circumstances.

ORCID

S. B. Beale https://orcid.org/0000-0002-6755-9111
S. Zhang https://orcid.org/0000-0002-8645-6003
A. A. Kulikovsky https://orcid.org/0000-0003-1319-576X

References

1. S. V. Patankar and D. B. Spalding, "A calculation procedure for the transient and steady-state behavior of shell-and-tube heat exchangers.", ed. N. Afgan and E. U. Schlünder *Heat Exchangers: Design and Theory Sourcebook* (Scripta Book Company, Washington. D.C.) 155 (1974).
2. D. Butterworth, "The development of a model for three-dimensional flow in tube bundles." *International Journal of Heat and Mass Transfer*, **21**, 253 (1977).
3. D. B. Rhodes and L. N. Carlucci, "Predicted and measured velocity distributions in a model heat exchanger." *Proceedings CNS/ANS International Conference on Numerical Methods in Nuclear Engineering AECL-8271*, Atomic Energy of Canada Ltd. (1984) 1–19.
4. V. M. Theodossiou and A. C. M. Sousa, "Flow field predictions in a model heat exchanger." *Computational Mechanics*, **3**, 419 (1988).
5. M. Prithiviraj and M. J. Andrews, "Three dimensional numerical simulation of shell-and-tube heat exchangers. Part I: Foundation and fluid mechanics." *Numerical Heat Transfer, Part A*, **33**, 799 (1998).
6. M. Prithiviraj and M. J. Andrews, "Three-dimensional numerical simulation of shell-and-tube heat exchangers. Part II: Heat transfer." *Numerical Heat Transfer, Part A*, **33**, 817 (1998).
7. B. Sundén, "Computational fluid dynamics in research and design of heat exchangers." *Heat Transfer Engineering*, **28**, 898 (2007).
8. H. Darcy, *Les fontaines publiques de la ville de Dijon: exposition et application des principes à suivre et des formules à employer dans les questions de distribution d'eau. Un appendice relatif aux fournitures d'eau de plusieurs villes au filtrage des eaux* (Victor Dalmont, Paris) 1 (1856).
9. O. Reynolds, "On the extent and action of the heating surface of steam boilers." *Proceedings of the Literary and Philosophical Society of Manchester*, **14**, 81 (1875).
10. S. B. Beale and S. V. Zhubrin, "A distributed resistance analogy for solid oxide fuel cells." *Numerical Heat Transfer, Part B: Fundamentals*, **47**, 573 (2005).
11. R. T. Nishida, S. B. Beale, J. G. Pharoah, L. G. J. de Haart, and L. Blum, "Three-dimensional computational fluid dynamics modelling and experimental validation of the Jülich Mark-F solid oxide fuel cell stack." *Journal of Power Sources*, **373**, 203 (2018).
12. M. Navasa, X.-Y. Miao, and H. L. Frandsen, "A fully-homogenized multiphysics model for a reversible solid oxide cell stack." *International Journal of Hydrogen Energy*, **44**, 23330 (2019).
13. S. Zhang, R. Peters, B. Varghese, R. Deja, N. Kruse, S. Beale, L. Blum, R. Peters, and R.-A. Eichel, "Modeling of reversible solid oxide cell stacks with an open-source library." *J. Electrochem. Soc.*, **169**, 114501 (2022).
14. S. Zhang, "Modeling and simulation of polymer electrolyte fuel cells." *PhD thesis, RWTH Aachen* (2019).
15. Z. J. He, H. Li, and E. Birgersson, "Reduced model for the planar solid oxide fuel cell." *Computers & Chemical Engineering*, **52**, 155 (2013).
16. Z. He, E. Birgersson, and H. Li, "Reduced non-isothermal model for the planar solid oxide fuel cell and stack." *Energy*, **70**, 478 (2014).
17. L. Chen, R. Zhang, T. Min, Q. Kang, and W. Tao, "Pore-scale study of effects of macroscopic pores and their distributions on reactive transport in hierarchical porous media." *Chemical Engineering Journal*, **349**, 428 (2018).
18. M. Engelbracht, R. Peters, L. Blum, and D. Stolten, "Analysis of a solid oxide fuel cell system with low temperature anode off-gas recirculation." *J. Electrochem. Soc.*, **162**, F982 (2015).
19. R. Peters, R. Deja, Q. Fang, V. N. Nguyen, P. Preuster, L. Blum, P. Wasserscheid, and D. Stolten, "A solid oxide fuel cell operating on liquid organic hydrogen carrier-based hydrogen - A kinetic model of the hydrogen release unit and system performance." *International Journal of Hydrogen Energy*, **44**, 13794 (2019).
20. O. Furst and O. Deutschmann, "Development and calibration of a fast flow model for solid oxide cell stack internal manifolds." *Journal of Power Sources*, **613**, 234857 (2024).
21. L. Wehrle, D. Schmider, J. Dailly, A. Banerjee, and O. Deutschmann, "Benchmarking solid oxide electrolysis cell-stacks for industrial Power-to-Methane systems via hierarchical multi-scale modelling." *Applied Energy*, **317**, 119143 (2022).
22. C. Yang, Z. Li, Y. Jin, Y. Wang, Y. Wu, H. Miao, and J. Yuan, "Modeling and analysis of the multiphysics transport parameters of a kilowatt-class multistack module of reversible solid oxide cells." *Applied Thermal Engineering*, **235**, 121373 (2023).
23. J. Fan, J. Shi, Y. Wang, and Y. Shi, "Numerical investigation of air flow characteristics for a compact 5 x 10 array tubular segmented-in-series solid oxide fuel cell stack." *Applied Thermal Engineering*, **247**, 123039 (2024).
24. Z. Yang, K. Jiao, Z. Liu, Y. Yin, and Q. Du, "Investigation of performance heterogeneity of PEMFC stack based on 1+1D and flow distribution models." *Energy Conversion and Management*, **207**, 112502 (2020).
25. A. Omran, A. Lucchesi, D. Smith, A. Alaswad, A. Amiri, T. Wilberforce, J. R. Sodré, and A. G. Olabi, "Mathematical model of a proton-exchange membrane (PEM) fuel cell." *International Journal of ThermoFluids*, **11**, 100110 (2021).
26. B. Hu, Z. Qu, J. Zhang, X. Wang, H. Sun, and Y. Wang, "Operating performance and energy flow modeling for a hundred-kilowatt proton exchange membrane fuel cell stack test system." *Applied Energy*, **372**, 123851 (2024).
27. C. Yang, Z. Li, Y. Wang, H. Miao, and J. Yuan, "Multiphysics analysis of flow uniformity and stack/manifold configuration in a kilowatt-class multistack solid oxide electrolysis cell module." *Energy*, **307**, 132627 (2024).
28. L. Wehrle, A. Ashar, O. Deutschmann, and R. J. Braun, "Evaluating high power density, direct-ammonia SOFC stacks for decarbonizing heavy-duty transportation applications." *Applied Energy*, **372**, 123646 (2024).
29. C. Gong, L. Xing, C. Liang, and Z. Tu, "Modeling and dynamic characteristic simulation of air-cooled proton exchange membrane fuel cell stack for unmanned aerial vehicle." *Renewable Energy*, **188**, 1094 (2022).
30. R. Peters, N. Kruse, W. Tiedemann, I. Hoven, R. Deja, D. Schäfer, F. Kunz, and R.-A. Eichel, "Layout and Experimental Results of an 10/40 Kw rSOC Demonstration System." *ECS Trans.*, **111**, 1657 (2023).
31. N. Kruse, W. Tiedemann, I. Hoven, R. Deja, R. Peters, F. Kunz, and R.-A. Eichel, "design and experimental investigation of temperature control for a 10 kw SOFC system based on an artificial neuronal network." *ECS Trans.*, **111**, 493 (2023).
32. S. B. Beale, "Mass transfer in plane and square ducts." *International Journal of Heat and Mass Transfer*, **48**, 3256 (2005).
33. S. B. Beale and A. Kumar, "Fluid dynamics of spacer filled rectangular and curvilinear channels." *Journal of Membrane Science*, **271**, 1 (2006).
34. S. B. Beale, J. G. Pharoah, and A. Kumar, "Numerical study of laminar flow and mass transfer for in-line spacer-filled passages." *Journal of Heat Transfer*, **135**, 011004 (2013).
35. L. Gurreri, A. Tamburini, A. Cipollina, G. Micale, and M. Ciofalo, "Pressure drop at low Reynolds numbers in woven-spacer-filled channels for membrane processes: CFD prediction and experimental validation." *Desalin. Water Treat*, **61**, 170 (2017).
36. D. A. Drew and S. L. Passman, *Theory of multicomponent fluids* (Springer Science & Business Media, New York) vol. 135 (2006).
37. R. K. Shah and A. L. London, "Laminar flow forced convection in ducts.", ed. T. Irvine and J. Hartnett *Advances in Heat Transfer* (Academic Press, New York)book section VII, 196 (1978).
38. S. B. Beale, "A simple, effective viscosity formulation for turbulent flow and heat transfer in compact heat exchangers." *Heat Transfer Engineering*, **33**, 4 (2012).
39. M. Jacob, *Heat Transfer* (Wiley, New York) (1949).
40. A. S. Berman, "Laminar flow in channels with porous walls." *J. Appl. Phys.*, **24**, 1232 (1953).
41. W. M. Kays, M. E. Crawford, and B. Weigand, *Convective Heat and Mass Transfer, 4th Edition* (McGraw-Hill, New York) (2005).
42. A. F. Mills, *Mass Transfer* (Prentice Hall, Upper Saddle River, N.J.) (2001).
43. J. Jorne, "Mass-transfer in laminar-flow channel with porous wall." *J. Electrochem. Soc.*, **129**, 1727 (1982).
44. S. B. Beale, A. Ginolin, R. Jerome, M. Perry, and D. Ghosh, "Towards a virtual reality prototype for fuel cells." *PHOENICS Journal of Computational Fluid Dynamics and its Applications*, **13**, 287 (2000).
45. A. A. Kulikovsky, "Laminar flow in a PEM fuel cell cathode channel." *J. Electrochem. Soc.*, **170**, 024510 (2023).
46. A. A. Kulikovsky, "The effect of stoichiometric ratio λ on the performance of a polymer electrolyte fuel cell." *Electrochimica Acta*, **49**, 617 (2004).

47. A. A. Kulikovsky, A. Kucernak, and A. A. Kornyshev, "Feeding PEM fuel cells." *Electrochimica Acta*, **50**, 1323 (2005).
48. S. B. Beale, "A simple electrochemical cell model." *Electrochemical Cell Calculations with OpenFOAM*, ed. S. Beale and W. Lehnert (Springer Nature, Switzerland) Lecture Notes in Energy, 42, 21–57 (2022).
49. P. Lessner and J. Newman, "Hydrodynamics and mass-transfer in a porous-wall channel." *J. Electrochem. Soc.*, **131**, 1828 (1984).
50. R. T. Nishida, S. B. Beale, and J. G. Pharoah, "Comprehensive computational fluid dynamics model of solid oxide fuel cell stacks." *International Journal of Hydrogen Energy*, **41**, 20592 (2016).
51. S. B. Beale, H. W. Choi, J. G. Pharoah, H. K. Roth, H. Jasak, and D. H. Jeon, "Open-source computational model of a solid oxide fuel cell." *Comput. Phys. Commun.*, **200**, 15 (2016).
52. B. Poling, J. Prausnitz, and J. Connell, *The Properties of Gases and Liquids* (McGraw-Hill, New York) (2001).
53. C. R. Wilke, "A viscosity equation for gas mixtures." *The Journal of Chemical Physics*, **18**, 517 (1950).
54. M. Ishii, *Drift-flux model and constitution equations for relative motion between phases in various two-phase flow regimes Report ANL-77-47*, Reactor Analysis and Safety Division, Argonne National Laboratory (1977).
55. C. Wang and P. Cheng, "A multiphase mixture model for multiphase, multicomponent transport in capillary porous media—I. Model development." *International Journal of Heat and Mass Transfer*, **39**, 3607 (1996).
56. T. Sherwood, P. Brian, and R. Fisher, *Salt concentration at phase boundaries in desalination processes 295-1*, Desalination research laboratory, Massachusetts Institute of Technology (1963).
57. T. K. Sherwood, P. L. T. Brian, R. E. Fisher, and L. Dresner, "Salt concentration at phase boundaries in desalination by reverse osmosis." *Industrial & Engineering Chemistry Fundamentals*, **4**, 113 (1965).
58. S. Chellam, M. R. Wiesner, C. Dawson, and G. R. Brown, "Laminar flow in porous ducts." *Reviews in Chemical Engineering*, **11**, 53 (1995).
59. B. K. Gupta and E. K. Levy, "Laminar flow in annuli and flat plate channels with mass transfer at one wall.", ed. M. M. Yovanovich *Heat Transfer with Thermal Control Applications, Technical Papers Selected from AIAA/ASME 1974 Thermophysics and Heat Transfer Conference, American Institute of Aeronautics and Astronautics* 167 (1975).
60. G. S. Beavers, E. M. Sparrow, and R. A. Magnuson, "Experiments on coupled parallel flows in a channel and a bounding porous medium." *Journal of Basic Engineering*, **92**, 843 (1970).